THE UNIVERSITY of EDINBURGH

Edinburgh Research Explorer

Extracting mud invasion information using borehole radar-a numerical study

OPEN ACCESS

GEOPHYSICS®

Extracting mud invasion information using borehole radar--- a numerical study

Journal:	*Geophysics*
Manuscript ID	GEO-2022-0121.R2
Manuscript Type:	Technical Paper
Keywords:	borehole geophysics, ground-penetrating radar (GPR)
Manuscript Focus Area:	Ground-Penetrating Radar

SCHOLARONE™
Manuscripts

Extracting mud invasion information using borehole radar—a numerical study

(October 14, 2022)

Running head: **Borehole radar evaluating mud invasion**

ABSTRACT

In hydrocarbon drilling, mud filtrate penetrates permeable formations, and alters the pore fluid characteristics in the immediate vicinity of the borehole. Typically, the prevailing in-situ pore fluids are displaced by the invading mud filtrate, which leads to gradually changing distributions of the fluid and electrical properties. Understanding this invasion process is crucial for the interpretation of logging data and associated reservoir evaluations. Conventional logging methods tend to be inadequate for this purpose as their resolution is too low. We show that invasion depth can be determined from borehole radar data using an optimized antenna configuration and time-lapse measurements. A series of parametric sensitivity analyses provide information about the effects of variations of the rock and fluid properties on the identification and extraction of borehole radar signals reflected from the invasion front. Our results suggest that by embedding the radar antennas in cavities filled with an absorbing dielectric material, it is possible to minimize the interference arising from the metal components of the logging tool. In the simulated reservoir scenario, a time-lapse measurement mode with a time interval of at least 6 hours can reliably extract the radar signals reflected from the invasion front, and the proposed borehole radar has a lateral detection range from 0.15 to 1 m. A comprehensive range of parametric sensitivity analyses indicate that the signals reflected from the invasion front are principally influenced by oil

viscosity, porosity, and mud and formation water salinity, as well as by molecular diffusion coefficient and cementation exponent. These properties and parameters should be carefully explored and assessed when applying borehole radar to evaluate mud invasion information in a reservoir environment.

INTRODUCTION

In hydrocarbon drilling, mud is injected into the borehole to provide a higher downhole pressure with respect to the formation, and, thus, to maintain the stability of the borehole wall (Abrams, 1977). In response to this, the liquid part of the mud, known as the mud filtrate, penetrates into the permeable formations and displaces the in-situ pore fluids. The invaded mud infiltrate thus changes the petrophysical properties of the near-borehole formation, which complicates the interpretations of conventional logging data (Ning et al., 2013; Akinsete and Adekoya, 2016). This is so-called mud invasion phenomenon commonly encountered in drilling and logging (Crain, 2002). In this process of mud invasion, solid particles gradually deposit on the borehole wall and develop a mud cake, which, in turn, slows down the infiltration rate (Dewan and Chenvert, 1993; Amorin et al., 2019).

Logging engineers generally divide the mud-invaded reservoir into the flushed zone, the transition zone, and the virgin zone according to how much of the in-situ formation fluids have been displaced by the mud filtrate (Allen et al., 1991). Many attempts have been made to correct logging data contaminated by the effects of mud invasion, whereby the virgin formation properties are derived by eliminating the effects of the flushed and transition zones on logging signals (Fan et al., 2017; Zhao et al., 2019). To this end, it is crucial to adequately estimate the mud invasion status. A frequently used approach is to employ electrical logging tools, such as array induction logging and array lateral logging, for obtaining apparent electrical resistivity profiles and sequentially inferring the true resistivity as a function of the radial distance (Alpak et al., 2006). Three-parameter (resistivity of flushed zone, resistivity of virgin zone, and invasion depth) or five-parameter (resistivity of flushed zone, resistivity of low-resistivity annulus, resistivity of virgin zone, depth of

flushed zone, and depth of transition zone) inversion algorithms were proposed to roughly estimate the invasion profile by simplifying a gradually varying invasion distribution into several stepped annuli (Deng et al., 2012; Zhou et al., 2016). These inversion approaches are, however, intrinsically non-unique, which leads to considerable uncertainties or even errors in reservoir assessment and logging interpretations. The primary reason is that such low-frequency logging tools have fairly low spatial resolutions relative to the scale of the targeted fluid distributions. If some important characteristics of mud invasion, such as the invasion depth, are accurately determined, the non-uniqueness of the solutions can be alleviated or even eliminated, which, in turn, allows for an accurate estimation of the properties of the virgin formation. The invasion status has proven to exhibit a strong correlation with some hydrodynamic characteristics, notably the permeability and the porosity (Alpak et al., 2006). This correlation allows for estimating some key petrophysical properties once the invasion depth is accurately derived (Torres-Verdín et al., 2006). Furthermore, the invasion depth as a function of time is linked to predicting oil productivity because water-based mud invading an oil-bearing layer obeys a very similar displacement mechanism as the one prevailing during water-flooding recovery (Zhang et al., 2005). Consequently, it is of vital importance to develop a high-resolution logging method to characterize the mud invasion status.

Ground-penetrating radar (GPR), an electromagnetic (EM) exploration method that works at frequencies ranging from megahertz to gigahertz, has been widely applied to near-surface geophysical surveys (Jol, 2009). Conventional surface-based GPR has a limited investigation depth and hence, borehole radar has been developed to allow for placing radar antennas in a borehole closer to a target (Slob et al., 2010). To date, borehole radar has been successfully applied to mineral exploration (Pisani and Vogt, 2004), cavity imaging

(Tronicke and Hamann, 2014), fracture characterizing (Zhou and Sato, 2004), and hydroge-

ological investigations (Jang et al., 2011). In the past two decades, several theoretical and

experimental studies have been carried out to investigate the feasibility of applying borehole

radar to well logging (Liu and Sato, 2002; Chen and Oristaglio, 2002; Heigl and Peeters,

2005), as well as to some other hydrocarbon related applications (Miorali et al., 2011b,a;

Oloumi et al., 2015; Zhou et al., 2018, 2020). Among the various application scenarios,

borehole radar logging is the one for which hardware has been developed in field trials (Huo

et al., 2014, 2021). This borehole radar logging prototype, whose original purpose was to

detect caves and fractures in carbonate reservoirs, operates at a center frequency of 225

MHz, with a spatial resolution of few decimeters and a penetration range of several meters

in typical hydrocarbon reservoirs (Ma et al., 2016). If the operating frequency of borehole

radar logging tools is increased further, their spatial resolution can adequately characterize

the detailed structure of the formation in the immediate vicinity of the borehole wall. In

mud-invaded formations, borehole tools with a penetration of tens of centimeters and a ra-

dial resolution of few centimeters are needed for adequately describing the complex invasion

profile. Heigl and Peeters (2005) conducted a numerical study to investigate high-frequency

EM wave propagation and scattering phenomena in a mud-invaded formation. Their results

suggested that a borehole radar with a center frequency of 1 GHz can receive discernable

signals reflected from the invasion front with relatively narrow constraints imposed on the

formation properties and on the radar system performance. Although their study oversim-

plified the invasion process into a piston-like displacement, the proposed operating frequency

provides useful guidelines for further developments. Inspired by their work, we have pro-

posed a borehole radar measurement strategy for permeability estimation, where a borehole

radar tool with an operating frequency of 1 GHz is deployed in a mud-filled borehole to

detect the invasion front (Zhou et al., 2020). The derived invasion depth was subsequently associated with the permeability for reservoir evaluation. The results of this numerical study showed that the estimated permeability agreed well with the underlying hydraulic model, pointing to the promise of borehole radar applications in hydrocarbon reservoirs.

Although our previous study provided encouraging results, it also revealed that the accuracy of the permeability estimation relies heavily on the accuracy with which the EM signals reflected from invasion front can be extracted. The challenges primarily reside in the complicated downhole environments and the gradually varying fluid distributions, which exert a significant impact on EM wave propagation. Meanwhile, the diversity of reservoir types imposes considerable limitations or even risks on the practical applications of borehole radar logging. These considerations motivate us to further investigate the borehole radar configurations and working modes, and to analyze the influence of rock and fluid properties on recorded signals.

This paper investigates the effects of borehole radar configurations, measurement modes and petrophysical properties on the EM signals reflected from the invasion front. The study is carried out through numerical simulations, where a coupled multi-phase fluid flow and EM wave propagation model is used to assess the borehole radar responses of mud invaded formations in a wide range of but realistic scenarios. By changing the settings of some key downhole parameters and measurement variables, an optimized antenna configuration and measurement mode is recommended. By perturbing a wide range of rock and fluid properties and observing their respective effects on the signals reflected from the invasion front, the crucial properties dominating the signal quality are assessed and suitable reservoir environments for the corresponding applications are identified. The work in this paper expects to provide a guideline for future applications of borehole radar in oil fields.

6

METHODOLOGY

Numerical modeling

A coupled multi-phase fluid flow and EM wave propagation model is established to simulate borehole radar data acquisition in a mud-invaded formation. The borehole radar model is established using gprMax, a general-purpose finite-difference time-domain EM simulator (Warren et al., 2016). The simulation domain has a dimension of 1 m $\times$ 0.15 m $\times$ 0.7 m, and contains the mud-invaded zones and the borehole. The model is bounded by the absorbing boundary conditions using so-called first order complex frequency shifted perfectly matched layers (Warren et al., 2016). The radar antennas are modeled as Hertz dipole point sources placed inside the cavities of a logging tool. The transmitting antenna is excited by a Ricker wavelet with a center frequency of 1 GHz and a bandwidth of approximately 3 GHz. The cells have a dimension of 0.002 m $\times$ 0.002 m $\times$ 0.002 m.

The mud invasion process corresponds to the displacement of oil and brine under the pressure difference prevailing between the borehole and the formation. This displacement process is accompanied by the convection and diffusion of ions, which, in turn, alters the composition of the pore fluids and, thus, the bulk conductivity and permittivity of the formation. This process can be described by the two-phase flow and convection-diffusion equations, which are described by Equations 1-9 in Appendix A. The mud cake is a crucial part of this process as it dominates the invasion rate (Salazar and Torres-Verdín, 2008). A set of empirical formulas describing the changes of the mud cake properties, which have been derived from physical experiments, are coupled to the fluid model. These formulas, which are described in Equations 10-13 of Appendix A, emulate the dynamic evolution of the thickness, permeability, and porosity of the mud cake over time (Wu et al., 2005). Af-

ter discretization by the finite-difference time-domain method, the considered mud invasion

model can simulate the evolution of the pressure, saturation, and salinity. To observe the

response of the borehole radar with regard to the mud invasion process, it is essential to

convert the rock and fluid properties into electrical properties. We use Archie's law and the

Complex Refractive Index Model (CRIM), which are commonly used for the descriptions

of the electrical properties in sandstone reservoirs (Chen and Oristaglio, 2002; Heigl and

Peeters, 2005; Miorali et al., 2011a,b; Zhou et al., 2018, 2020), to calculate the bulk con-

ductivity and the bulk dielectric permittivity of the saturated rock (Archie, 1942; Bateman

and Konen, 1978; Birchak et al., 1974). Temperature and salinity effects on the electrical

properties in deep reservoir environments are accounted for through Equations 14-17 of

Appendix A.

Reservoir scenario

A synthetic reservoir scenario is used to simulate borehole radar measurements in a mud-

invaded hydrocarbon reservoir. The reservoir consists of sandstone with a porosity of 15 %,

a water saturation of 30 %, and a permeability of 3 md. The salinities of the formation water

and the mud filtrate are 120×10^3 ppm and 1×10^3 ppm, respectively. The saturation and

salinity properties are typical for freshwater-based mud invading a layer saturated by oil and

brine. The viscosities of oil and water are 3.550 cp and 1.274 cp, respectively, with the former

being typical of a conventional light oil reservoir. The pore surface is assumed as water-wet,

and is principally characterized by capillary pressure and relative permeability. The relative

permeability and capillary pressure are functions of water saturation (Delshad and Pope,

1989). Mud cake evolution is primarily controlled by the mud compositions in addition to

the pressure difference between the borehole and the reservoir, as described by Equations 10-

13 of Appendix A. These mud parameters can be acquired from an appropriately designed

mud filtration test (Dewan and Chenvert, 1993). The bulk conductivity and permittivity

of the saturated rock are determined by the conductivity and permittivity of oil, water and

rock and their respective volume fractions through Archie's law and the CRIM formula. The

materials in the reservoir are treated as frequency-independent at the considered operating

frequency and bandwidth of the borehole radar. The permittivity of water is assumed to be

real-value and assigned a lower value in deep reservoir environments compared to its surficial

value. Laboratory measurements have shown that as the temperature increases, the real

part of the complex permittivity of water drops gradually, and the relaxation frequency of

water rises (Hizem et al., 2008). For the temperature and operating frequency considered in

this study, the imaginary part of the permittivity of water can be neglected, and the value

of water permittivity is estimated by interpolating the experimental data (Hizem et al.,

2008; Zhou et al., 2020). Table 1 summarizes the properties and parameters of the fluids,

mud cake, borehole and rock considered in this study.

[Table 1 about here.]

Antenna configurations

In the process of mud invasion, the invasion front presents a significant contrast of the

electrical properties, and, hence, may generate detectable EM wave reflections. In this

study, a one-transmitter and two-receiver antenna configuration scheme is considered in the

downhole measurement. This measurement mode is designed to convert the travel time of

the received EM waves into the invasion depth, as described in Zhou et al. (2020). The

offsets of the transmitter and receivers are comparable with the invasion depth (Figure 1).

[Figure 1 about here.]

To apply borehole radar in a reservoir environment, two issues need to be carefully addressed when designing corresponding logging tools. One is to prevent the conductive mud from the emitted high-frequency EM signals, and the other is to minimize the EM interference with the metal components of the logging tools. A backward caliper is hinged with the logging tool to push the antennas against the borehole wall, thereby reducing the EM attenuation from the conductive mud. Half-cylindrical cavities are made in the logging tool for the installation of the radar antennas, and the cavities are filled with a special type of absorbing material to absorb the backward radiated EM waves. Normally, such backward radiated EM waves are not completely absorbed, and, hence, 'ringing' phenomenon may persist (Annan, 2009). This, in turn, may reduce detectability of weak reflected signals. A ferrite-type absorbing material is recommended for the borehole radar in this study, because it has high mechanical strength as well as high dielectric and magnetic losses in the pertinent frequency band (Chen et al., 2002). The dielectric properties of the absorbing material employed in this model emulate the sintered nickel zinc ferrite (Liu, 2014), and the absorbing effects in the considered radar frequency range have proven highly effective (Zhou et al., 2020).

To further improve the source, it is necessary to investigate the effects of the sizes of the cavities on the waveforms for the considered absorbing material. We change the radial depth and longitudinal length of the antenna cavities, respectively, and simulated the borehole radar transmitting EM wave in a homogeneous formation. Figures 2 and 3 show the waveforms recorded by the two receiving antennas. It is important to note that, in this paper, the amplitudes of the EM waves are displayed using a logarithmic scale,

which is beneficial for the visual comparison between the strong direct wave and the weak

reflected events. From these figures, it can be seen that there are some trailing signals

following the direct wave, which are the ringing effects caused by the reverberations in the

cavities. The comparisons of the waveforms show that with increasing radial depth and

longitudinal length of the antenna cavities, the ringing effects gradually become weaker,

whereas amplitude of the direct waves remains largely unaffected. The comparisons suggest

that once the absorbing material is determined, large antenna cavities are recommended

provided that the mechanical strength of the logging tool allow for it. In this study, the

preferred antenna cavities in the logging string have a longitudinal length of 20 cm and a

radial depth of 6 cm (Figure 1). The principal geometric parameters and dielectric properties

of the borehole radar tool are described in Table 2.

[Figure 2 about here.]

[Figure 3 about here.]

[Table 2 about here.]

SURVEY METHOD

Time-lapse measurements

When applying borehole radar to estimate the invasion depth, it is of vital importance to

exactly extract the reflections from the invasion front. However, the signals reflected from

the invasion front are weak relative to the direct wave, and, thus, the extraction method

is a matter of concern. Working in a deep downhole environment, borehole radar suffers

less from ambient noise than surface-based GPR. Therefore, much attention is paid to the

clutter arising from the heterogeneous distributions of the fluid and rock properties, which

lower the signal quality and may make straightforward extractions of useful signals difficult

or even impossible. A potential solution is to adopt a time-lapse measurement mode, which

keeps the antennas at the same position and sequentially collects radar data twice with a

time interval of few hours. Between the two measurements, the invasion front moves forward

over time, which creates changed signals in the two sets of data. Meanwhile, the virgin zone

and the flushed zone remain almost unchanged over the measurement time, which results in

negligible changes in the time-lapse data. A subtraction operation is subsequently applied

to the two sets of data, which removes the majority of the background signals and only

retains the parts of the signals that have changed. Similar time-lapse GPR survey methods

have been applied to soil water evaluation (Klotzsche et al., 2019), contaminated water

detection (Daniels et al., 1995), oil production monitoring (Zhou et al., 2018), and some

other fluid flow-related scenarios.

Figure 4 shows the radial distributions of the fluid properties after an invasion time of

72 and 96 hours, respectively. In the conductivity profile obtained after 72 hours, a sudden

rise occurs at a radial distance of 0.5 m, which corresponds to the location of the salinity

front. This contrast in conductivity is considered to be the main cause for the reflection

events. Over time, the invasion front moves farther away from the borehole wall, whereas

the flushed zone does not demonstrate observable changes. Figure 5 shows the original

EM waves recorded by the two receiving antennas after the invasion of 72 (black curves)

and 96 hours (blue curves), and their corresponding time-lapse differences (red curves),

respectively. As seen from the graph, in the two original waves, the strong direct waves are

overlapping, and the weak reflected waves are almost invisible, which makes it difficult to directly extract useful signals from the original radar data. Apart from the large amplitude difference, some trailing signals, which are caused by the heterogeneity of the formation, are mixed with the reflected signals and increase the difficulty of the signal extraction. After time-lapse subtraction operations, there are two events that remain in the waveforms. The earlier event denotes the residual direct waves arising from the slight changes of the flushed zones at the two measurement times, and the later one corresponds to the signals reflected from the invasion front at the first measurement time (i.e., 72 hours in this case). The second event is the desired signal related to the invasion depth, while the first event is not related to the invasion depth. In principle, a third event should be present corresponding to the reflections from the invasion front at the later measurement time. However, this signal encounters greater attenuation than the earlier one due to the larger propagation distance and is not always clearly observed. Therefore, in this study, the useful signals extracted through the time-lapse operations refer to the reflection observed in the first measurement time (hereinafter referred to as reflected waves or reflected signals).

[Figure 4 about here.]

[Figure 5 about here.]

From the time-lapse waveforms in Figure 5, it can be seen that the majority of the undesired wavelets are removed and relatively clean reflected waves are retained. Therefore, it seems feasible to employ time-lapse borehole radar to obtain the reflected signals from the invasion front. A practical challenge remains because an elaborate data acquisition operation is required to ensure the highly accurate location of borehole radar antennas for

the sequential measurements (Allroggen et al., 2020). This technical issue will be specifically addressed in future work.

Time interval of time-lapse measurements

Time-lapse measurements require at least two sequential operations at a certain time interval. It is therefore worthy of investigating how the lag time influences the signal extraction. To this end, we assume that the first measurement is conducted at an invasion time of 72 hours, and the second 2 to 24 hours later. Figures 6 and 7 show the radial distributions of the fluid properties at two measurement times and the corresponding time-lapse radar signals, respectively. This comparison reveals that, when the sequential measurements have a relatively short time interval (less than 4 hours), the reflected signals in the time-lapse data exhibit weak differences in terms of amplitude and phase. This problem can be alleviated using longer time intervals (longer than 6 hours in this case). That is because an intact reflected waveform can only be extracted from the two datasets when a sufficiently large spatial separation between the invasion fronts is present. In practice, the EM wavelength of the borehole radar and the migration velocity of the invasion front should be estimated and predicted for a given reservoir prior to the time-lapse measurement operations. For the determined measurement time interval, the separation of the invasion fronts should be comparable with or slightly larger than the wavelength of borehole radar, thus ensuring that the reflected signals can be accurately separated. In this paper, a measurement time interval of 24 hours is selected for following simulations.

[Figure 6 about here.]

[Figure 7 about here.]

14

Detection range

As discussed above, to successfully extract the reflected waves from the time-lapse signals, there must be a temporal separation between the direct and reflected waves. This, in turn, imposes a limitation on the minimum detection depth because an excessively shallow invasion depth tends to bring about this undesired overlap. We simulate a series of time-lapse borehole radar signals by varying the invasion depth at the first measurement from 1 m to 0.10 m, respectively. The measurement interval time is 24 hours as stated above. The simulated results imply that in the current scenario, when the invasion depth at the first measurement is shallower than 0.15 m, as shown in Figure 8c, it is difficult to distinguish the reflected wavelets from the residual direct waves in the time-lapse signals received by the farther receiving antenna (R_2) (Figure 9b). If it is required to detect an invasion depth shallower than 0.15 m, a potential solution is to configure an additional monostatic antenna in the transmitter to receive separable signals (Figure 9c). However, this kind of antenna configuration increases the costs and complexity of the downhole systems.

[Figure 8 about here.]

[Figure 9 about here.]

Generally, the invasion depth of interest is within 1 m. To check the capability of detecting weak reflected signals, a key indicator of GPR systems is the dynamic range, which corresponds to the logarithmic ratio of the maximum receivable and minimum detectable signal amplitudes (Jol, 2009). We simulate the time-lapse EM signals reflected from the invasion front at 1 m distance from the borehole wall (Figures 10 and 11). Assuming that the maximum recordable signal (i.e., saturated voltage) has an amplitude of 1 V/m, a

dynamic range of 96 dB is required in order to obtain the weak reflected signals shown in Figure 11. This can be achieved by using a 16-bit A/D sampling chip (Hamran et al., 1995). Consequently, our simulation results indicate that the current hardware has potential of supporting the borehole radar to detect the invasion front at a distance of approximately 0.15 to 1 m from the borehole wall.

[Figure 10 about here.]

[Figure 11 about here.]

SENSITIVITY ANALYSES OF PETROPHYSICAL PROPERTIES

In the process of mud invasion, the properties of the fluids and rocks influence the features of the invasion front, and therefore affect the propagation and reflection of EM waves. It is of vital importance to analyze the influence extent of a range of petrophysical properties on the signal quality of time-lapse borehole radar. The sensitivity analyses aim to screen out those properties that exert dominant effects on the extraction of the invasion front-reflected signals. The analyses help to determine reservoir types suitable for mud invasion detection using borehole radar.

The reservoir model, as described above, is used as a base scenario for parametric sensitivity analyses. The first measurement is made when the invasion front is at a distance of 0.4 m from the borehole wall, and the second measurement 24 hours later. We run a sequence of simulations by exerting independent perturbations on the petrophysical properties of the reservoir model, and observed the associated radial distributions of fluid and electrical properties as well as the resulted time-lapse borehole radar signals. The properties

that have the strong and weak influence on time-lapse signal extractions are summarized in Table 3. With regard to fluid flow, the major properties that influence signal extraction are those with great sensitivity to the electrical conductivity of the invasion profile. In the following, we consider several typical properties, observe their effects on reflected signals, and analyze the mechanism.

[Table 3 about here.]

Effects of viscosity

Viscosity provides a measure of the internal resistance to fluid flow (Andrade, 1930). In reservoir types, oil viscosity exhibits large differences, ranging from one tenth up to millions of times of the water viscosity (Beggs and Robinson, 1975). In this study, the oil viscosity is increased from 3.55 cp to 35.5 cp and 355 cp, respectively, thus simulating light, viscous, and heavy types of oil. The simulated fluid distributions and time-lapse EM signals are shown in Figures 12 and 13, respectively. It can be seen that the light oil reservoir (base case) presents a piston-like invasion profile (Figures 12a) and results in prominent EM reflections (Figure 13). Conversely, the viscous and heavy oils present gradually varying invasion zones (Figures 12a) and generate weakened but still detectable EM reflected waves (Figure 13). These results imply that the proposed method has a wide range of applications to various reservoir types, with light oil reservoirs presenting the best results.

[Figure 12 about here.]

[Figure 13 about here.]

Effects of porosity

Porosity tends to have a negative correlation with the invasion depth if its association with permeability is not considered (Zhou et al., 2015). In addition, it exerts significant influences on the electrical properties of the invaded formation according to Equations equations (14) and (16) of Appendix A. We run simulations by increasing the reservoir porosity from 0.15 to 0.25 and 0.35, respectively, thus representing three types of reservoirs (Salazar and Torres-Verdín, 2008). Dramatic changes are observed in the bulk conductivity and bulk permittivity profiles (Figures 14c and d) associated with corresponding changes in the amplitude and phase delays of the time-lapse EM signals (Figure 15). These phenomena are essentially caused by the rising bulk conductivity and permittivity (Figures 14c and d), which increase the propagation loss and decrease the wave velocity in the reservoir. The results reveal that a reservoir with a lower porosity is more favorable for extracting the signals reflected from the invasion front than the one with a higher porosity.

[Figure 14 about here.]

[Figure 15 about here.]

Effects of formation water salinity

The mud invasion process is treated as a multi-phase and multi-component flow problem (Torres-Verdín et al., 2006). Viewed from a microscopic perspective, when the mud filtrate flows into the formation, the invaded salt ions displace the in-situ salt ions under the actions of the convection and diffusion. As a result, the bulk conductivity of the formation is altered and a conductivity contrast is formed, which has the potential to generate EM

wave reflections. We decrease the in-situ formation water salinity from 12×10^4 ppm to 5×10^4 ppm and 1.2×10^4 ppm, obtained the distributions of the fluid and electrical properties, and evaluated the corresponding time-lapse radar responses (Figures 16 and 17). It can be seen that as the salinity of the in-situ formation water decreases, the conductivity of the in-situ formation decreases, whereas the conductivity of the flushed zone remains almost unchanged, thus leading to a dramatic drop in the magnitude of the reflected signals. Note that the formation permittivity exhibits a slight rise as the formation water salinity increases. This phenomenon is caused by the dependence of the water salinity on the water permittivity (Equation 17). However, the slightly changed formation permittivity contributes little to the reflected waves and, thus, is neglected. These results imply that a high-salinity reservoir is ~~favorite~~ for the extraction of the reflected waves because the invasion is associated ~~by~~ a large electrical conductivity contrast.

[Figure 16 about here.]

[Figure 17 about here.]

Effects of heterogeneity

Realistic reservoirs are characterized by heterogeneity of petrophysical properties, which influence the distributions of fluids and electrical properties. To investigate the associated influence on time-lapse borehole radar signals, a fractal-type model is used to generate 3D heterogenous porosity distributions (Danos, 1997; Xia et al., 2019). It is acknowledged that there also exist heterogeneities in the initial water saturation and the permeability in addition to the porosity (Shenawi et al., 2007; Han et al., 2021). However, the inhomogeneity

of the permeability exerts straightforward influence on the fluid flow compared to the rock

electrical properties. The inhomogeneous water content distributions arising from the het-

erogeneity of the porosity are equivalent with the heterogeneous initial water saturation.

Therefore, this study neglects the heterogeneity of the permeability and initial water satu-

ration to simplify the modeling process. In the resulting heterogenous reservoir models, the

porosity distributions have a mean value of 0.15 (the same as in the base scenario) and a

variance of 0.03, i.e., the porosity fluctuates from 0.12 to 0.18. The variation is close to the

realistic range of the reservoir porosity, where the cavities and fractures are not present.

The fractal dimension is set to be 1, 2 and 3, respectively, representing three different types

of heterogeneities, as presented in Figures figures 18–20. Figure 21 presents the received

time-lapse borehole radar signals when the invasion front is at a distance of 0.4 m from

the borehole wall. The comparison of waveforms indicates that the time-lapse responses

obtained from the heterogeneous reservoirs almost overlap with those of the homogeneous

reservoir (base case). These observation indicates that the heterogeneity of the porosity

in the near-borehole regions does not have a strong impact on the signal quality of time-

lapse borehole radar measurements. The reasons are the following. On the one hand, it is

the uneven fluid distributions that govern the propagation and reflection of high-frequency

EM waves in reservoirs rather than the rock per se; on the other hand, the clutter arising

from the heterogeneities are filtered by the time-lapse subtraction operations. This, in turn,

points to the validation of assuming a homogeneous reservoir model in the above subsections

to implement the parametric sensitivity analyses.

[Figure 18 about here.]

[Figure 19 about here.]

[Figure 20 about here.]

[Figure 21 about here.]

CONCLUSIONS

This paper investigates the applicability of borehole radar for detecting the mud invasion based on a coupled mud invasion and borehole radar simulations. The results suggest that (1) a borehole radar with a center frequency of 1 GHz is ~~applicable~~ to detect mud invasion front; (2) within the logging string, radar antennas can be placed in cavities, filled by an absorbing material, with a depth and length of at least 6 cm and 20 cm, respectively, to diminish the ringing effects; (3) a time-lapse acquisition scheme is able to remove the majority of EM background signals and clutter, and allows to obtain relatively clean signals reflected from the invasion front; (4) a time interval larger than 6 hours is recommended in the time-lapse measurements to achieve an adequate separation of the time-lapse reflected signals; (5) under the assumed borehole configurations and reservoir environment, the detection range goes from approximately 0.15 to 1 m; (6) the signals reflected from the mud invasion front are primarily influenced by the oil viscosity, the porosity, the mud and formation water salinity, the molecular diffusion coefficient, and the cementation exponent, which are sensitive to the shape features of the conductivity profile of the invasion front. These properties and parameters should be carefully explored prior to the applications of the method to a given reservoir environment.

While our study suggests that borehole radar can be applied to the detection of the mud invasion front in a deep oil reservoir, the reservoir types and fluid properties should

21

be carefully analysed before conducting a practical downhole operation. Even though our numerical results indicate that time-lapse borehole radar is a promising method for mud invasion characterization, an important potential problem in practical operations is the sufficiently accurate localization of borehole radar antennas during the time-lapse measurements. Besides, a special antenna type that suits for the downhole mud detection should be designed in the future work.

APPENDIX A

MATHEMATICAL DESCRIPTION OF MUD INVASION

Multiphase and multicomponent fluid flow

The mud invasion process can be described as multiphase and multicomponent flow problem. The two-phase flow equations of oil and water describe the pressure and saturation changes over time based on the isothermal Darcy flow theory (Aziz, 1979)

$$\nabla \cdot \left[\frac{\rho_{\mathrm{w}} k k_{\mathrm{rw}}}{\mu_{\mathrm{w}}}(\nabla P_{\mathrm{w}} - \rho_{\mathrm{w}} g \nabla h)\right] = \frac{\partial(\phi \rho_{\mathrm{w}} S_{\mathrm{w}})}{\partial t}, \tag{1}$$

$$\nabla \cdot \left[\frac{\rho_{\mathrm{o}} k k_{\mathrm{ro}}}{\mu_{\mathrm{o}}}(\nabla P_{\mathrm{o}} - \rho_{\mathrm{o}} g \nabla h)\right] = \frac{\partial(\phi \rho_{\mathrm{o}} S_{\mathrm{o}})}{\partial t}, \tag{2}$$

$$P_{\mathrm{c}}(S_{\mathrm{w}}) = P_{\mathrm{o}} - P_{\mathrm{w}}, \tag{3}$$

$$S_{\mathrm{o}} = 1 - S_{\mathrm{w}}, \tag{4}$$

where ρ_{w} and ρ_{o} are the densities of water and oil ($\mathrm{kg/m^3}$), respectively, k is the bulk permeability ($\mathrm{m^2}$), k_{rw} and k_{ro} are the relative permeabilities of water and oil (dimensionless), respectively, g is the gravity acceleration ($\mathrm{m/s^2}$), h is the depth (m), μ_{o} and μ_{w} are the viscosities of water and oil (Pa·s), respectively, P_{w} and P_{o} are the pressures of water and

oil (Pa), respectively, ϕ is the porosity (fraction), S_w and S_o are the saturations of water

and oil (fraction), t is the invasion time (s), and P_c is the capillary pressure (Pa).

The relative permeabilities and the capillary pressure are functions of water saturation

and can be described as ~~following~~ (Delshad and Pope, 1989)

$$k_{\text{rw}} = k_{\text{rw}}^0 \left(\frac{S_\text{w} - S_{\text{wc}}}{1 - S_{\text{wc}} - S_{\text{or}}} \right)^{e_\text{w}}, \tag{5}$$

$$k_{\text{ro}} = k_{\text{ro}}^0 \left(1 - \frac{S_\text{w} - S_{\text{wc}}}{1 - S_{\text{wc}} - S_{\text{or}}} \right)^{e_\text{o}}, \tag{6}$$

$$P_\text{c} = P_\text{c}^0 \sqrt{\frac{\phi}{k}} \left(1 - \frac{S_\text{w} - S_{\text{wc}}}{1 - S_{\text{wc}} - S_{\text{or}}} \right)^{e_\text{p}}, \tag{7}$$

where k_{rw}^0 and k_{ro}^0 are the end-point relative permeabilities of water and oil phases (dimen-

sionless), respectively, S_{wc} and S_{or} are the connate water and irreducible oil saturations

(fraction), respectively, e_w and e_o are the empirical exponents for water and oil (dimension-

less), respectively, P_c^0 is the capillary pressure coefficient (Pa·cm), and e_p is the pore size

distribution empirical exponent (dimensionless).

The multicomponent aspect of the considered multi-phase flow problem characterizes

the miscibility of water with different salt concentrations, and can be described by the

convection-diffusion equation (George et al., 2003)

$$\nabla \cdot \left[\frac{\rho_\text{w} k k_{\text{rw}} C_\text{w}}{\mu_\text{w}} (\nabla P_\text{w} - \rho_\text{w} \mathbf{g} \nabla h) \right] + \nabla \cdot (\rho_\text{w} \phi S_\text{w} K_\text{D} \nabla C_\text{w}) = \frac{\partial (\phi \rho_\text{w} S_\text{w} C_\text{w})}{\partial t}, \tag{8}$$

where C_w is the water salinity (ppm), and K_D is the dispersion coefficient that includes the

effects of molecular diffusion and hydrodynamic dispersion (m^2/s), which is expressed by

$$K_\text{D} = D + \frac{\alpha_\text{L}}{\phi S_\text{w}} \frac{k k_{\text{rw}}}{\mu_\text{w}} \nabla P_\text{w}, \tag{9}$$

where D is the molecular diffusion coefficient (m^2/s), and α_L is the dispersivity (m). The

first term of Equation 8 stands for the salinity change in response to the convective transport

of water, and the second term represents the salinity variation due to the salt concentration difference.

Using the finite-difference time-domain method, the equations above are discretized in a cylindrical coordinate systems, and the radial distributions of the fluid pressure, saturation, and salinity over invasion time are obtained.

Mud cake development

The changes of the permeability and porosity of the mud cake over time are influenced by the pressure drop across the mud cake, as described by Wu et al. (2005)

$$k_{mc}(t) = \frac{k_{mc0}}{P_{mc}^{\nu}(t)}, \tag{10}$$

$$\phi_{mc}(t) = \frac{\phi_{mc0}}{P_{mc}^{\delta \cdot \nu}(t)}, \tag{11}$$

where k_{mc} and ϕ_{mc} are the mud cake permeability and porosity, respectively, P_{mc} is the pressure drop across the mud cake, k_{mc0} and ϕ_{mc0} are the referenced permeability and porosity of the mud cake, respectively, which are measured under a pressure difference of 6.9 kPa, and ν and δ are the dimensionless compressibility exponent and the multiplier reflecting the relationship between the permeability and porosity of the compressible mud cake, and are constrained through laboratory measurements.

The instantaneous invasion rate of mud filtrate is given by (Wu et al., 2005)

$$q_{mc}(t) = \frac{2\pi h \left[P_m - P_{w,N}(t) \right]}{\sum_{i=2}^{N-1} \frac{\ln(r_{i+1}) - \ln(r_i)}{\left(\frac{kk_{ro}}{u_o} \right)_i \left(\frac{P_{c,i}(t) - P_{c,i+1}(t)}{P_{w,i}(t) - P_{w,i+1}(t)} \right) + \left(\frac{kk_{ro}}{\mu_o} + \frac{kk_{rw}}{\mu_w} \right)_i} + \frac{\mu_{mc}}{k_{mc}(t)} \ln \left(\frac{r_w}{r_{mc}(t)} \right)}, \tag{12}$$

where q_{mc} is the instantaneous invasion rate (m^3/s), h is the thickness of the permeable layer (m), P_{m} is the downhole pressure (Pa), μ_{mc} is the viscosity of the mud filtrate (Pa·s), and r_{w} is the radius of the wellbore (m), r_{mc} is the inner radius of the mud cake annulus (m). Note that the subscript i ~~implies the serial number of the grids~~ after the flow model has been discretized, where $i=1$ denotes the grid of the mud cake, and $i=N$ stands for the grid of radial outer boundary of the modeled domain. The first and second terms in the denominator of Equation 12 denote the flow resistivities of the formation and the mud cake, respectively.

The growth of the mud cake thickness over time (i.e., the decreasing r_{mc} in Equation 12) can be expressed by (Wu et al., 2005)

$$\frac{dr_{\mathrm{mc}}(t)}{dt} = -\frac{f_{\mathrm{s}}}{(1-f_{\mathrm{s}})[1-\phi_{\mathrm{mc}}(t)]} \cdot \frac{q_{\mathrm{mc}}(t)}{2\pi\Delta h \cdot r_{\mathrm{mc}}(t)}, \tag{13}$$

where f_{s} is the volume fraction of the solid particles contained in the mud.

Electrical properties

To convert the fluid properties to their electrical equivalents, empirical formulas are used. Archie's law is a good approximation to calculate the bulk electrical conductivity in a saturated sandstone reservoir and it can be described by (Archie, 1942)

$$\sigma = \frac{\sigma_{\mathrm{w}}\phi^m S_{\mathrm{w}}^n}{\alpha}, \tag{14}$$

where σ and σ_{w} denote the bulk conductivities of the saturated rock and the formation water conductivity (S/m), respectively, m, n and α are the cementation exponent, saturation exponent and tortuosity factor (dimensionless), respectively, which are the empirical parameters measured on core samples. The formation water conductivity σ_{w} is calculated

as a function of temperature and salinity, as described by Bateman and Konen (1978)

$$\sigma_{\mathrm{w}} = [(0.0123 + \frac{3647.5}{C_{\mathrm{w}}^{0.995}})\frac{82}{1.8T + 39}]^{-1}, \tag{15}$$

where C_{w} and T denote the formation water salinity (ppm) and he temperature (°C).

The bulk permittivity is calculated with the permittivities of the dry rock matrix, water, and oil and their respective volume fractions through a petrophysical mixing formula known as complex refractive index model (CRIM) (Birchak et al., 1974)

$$\sqrt{\varepsilon} = \sqrt{\varepsilon_{\mathrm{m}}}(1 - \phi) + \sqrt{\varepsilon_{\mathrm{o}}}(\phi - \phi S_{\mathrm{w}}) + \sqrt{\varepsilon_{\mathrm{w}}}\phi S_{\mathrm{w}}, \tag{16}$$

where ε, ε_{m}, ε_{o}, and ε_{w} denote the bulk permittivities of the saturated rock and the respective permittivities of the dry rock matrix, oil, and water. In a deep reservoir environment, the permittivity of water is ~~prominently~~ influenced by the temperature and salinity. A polynomial interpolation function, based on the laboratory measurements by Donadille and Faivre (2015), is used to link the salinity variation with the relative permittivity of water at a temperature of 93.2 °C, as described by

$$\varepsilon_{\mathrm{w}} = 57.93 - 4.417 \times 10^{-16}C_{\mathrm{w}}^3 + 4.266 \times 10^{-10}C_{\mathrm{w}}^2 - 1.443 \times 10^{-4}C_{\mathrm{w}}. \tag{17}$$

REFERENCES

Abrams, A., 1977, Mud design to minimize rock impairment due to particle invasion: Journal of Petroleum Technology, **29**, 586–592.

Akinsete, O., and D. Adekoya, 2016, Effects of mud filtrate invasion on well log measurements: SPE Nigeria Annual International Conference and Exhibition, Society of Petroleum Engineers, 184308.

Allen, D., F. Auzerias, E. Dussan, P. Goode, T. S. Ramakrishnan, L. Schwartz, D. Wilkinson, E. Fordham, P. Hammond, and R. Williams, 1991, Invasion revisited: Oilfield Review, **33**.

Allroggen, N., D. Beiter, and J. Tronicke, 2020, Ground-penetrating radar monitoring of fast subsurface processes: Geophysics, **76**, no. 2, E21–E34.

Alpak, F. O., C. Torres-Verdín, and T. M. Habashy, 2006, Petrophysical inversion of borehole array-induction logs: Part I–Numerical examples: Geophysics, **71**, no. 4, F101–F119.

Amorin, R., P. O. Appau, and E. Osei, 2019, Evaluation of blended lime-stabilised spent synthetic-based drilling mud and cement for oil well cementing operations: Advances in Geo-Energy Research, **3**, 141–148.

Andrade, E., 1930, The viscosity of liquids: Nature, **125**, 309–310.

Annan, A. P., 2009, Electromagnetic principles of ground penetrating radar, *in* Jol, H. M. ed., Ground penetrating radar: Theory and applications: Elsevier, 3–37.

Archie, G. E., 1942, The electrical resistivity log as an aid in determining some reservoir characteristics: Transaction of American Institute of Mining, Metallurgical, and Petroleum Engineers, **146**, 54–62.

Aziz, K., 1979, Petroleum reservoir simulation: Applied Science Publishers.

Bateman, R. M., and C. E. Konen, 1978, The log analyst and the programmable pocket

calculator: The Log Analyst, **19**, 3–7.

Beggs, H. D., and J. R. Robinson, 1975, Estimating the viscosity of crude oil systems: Journal of Petroleum Technology, **27**, 1140–1141.

Birchak, J. R., C. G. Gardner, J. E. Hipp, and J. M. Victor, 1974, High dielectric constant microwave probes for sensing soil moisture: Proceedings of the IEEE, **62**, 93–98.

Chen, Y., R. T. Coates, and W. C. Chew, 2002, FDTD modeling and analysis of a broadband antenna suitable for oil-field imaging while drilling: IEEE Transactions on Geoscience & Remote Sensing, **40**, 434–442.

Chen, Y. H., and M. L. Oristaglio, 2002, A modeling study of borehole radar for oil-field applications: Geophysics, **67**, 1486–1494.

Crain, E. R., 2002, Crain's petrophysical handbook: Rocky Mountain House.

Daniels, J. J., R. Roberts, and M. Vendl, 1995, Ground penetrating radar for the detection of liquid contaminants: Journal of Applied Geophysics, **33**, 195–207.

Danos, M., 1997, Fractals and chaos in geology and geophysics: Wiley Online Library.

Delshad, M., and G. A. Pope, 1989, Comparison of the three-phase oil relative permeability models: Transport in Porous Media, **4**, 59–83.

Deng, S., Q. Sun, H. Li, N. Huo, and X. He, 2012, The sensitivity of the array resistivity log to mud filtrate invasion and its primary five-parameter inversion for improved oil water recognition: Petroleum Science, **9**, 295–302.

Dewan, J. T., and M. E. Chenvert, 1993, Mudcake buildup and invasion in low permeability formations: Application to permeability determination by measurement while drilling: SPWLA 34th Annual Logging Symposium, Society of Petroleum Engineers, SPWLA–1993–NN.

Donadille, J., and O. Faivre, 2015, Water complex permittivity model for dielectric logging:

SPE Middle East Oil and Gas Show and Conference, Society of Petroleum Engineers, SPE–172566–MS.

Fan, Y., Z. Wu, F. Wu, J. Wu, and L. Wang, 2017, Simulation of mud invasion and analysis of resistivity profile in sandstone formation module: Petroleum Exploration and Development, **44**, 1045–1052.

George, B. K., C. Torres-Verdin, M. Delshad, R. Sigal, F. Zouioueche, and B. Anderson, 2003, A case study integrating the physics of mud-filtrate invasion with the physics of induction logging: Assessment of in-situ hydrocarbon saturation in the presence of deep invasion and highly saline connate water: Presented at the SPWLA 44th Annual Logging Symposium, Society of Petrophysicists and Well-Log Analysts.

Hamran, S. E., D. T. Gjessing, J. Hjelmstad, and E. Aarholt, 1995, Ground penetrating synthetic pulse radar: Dynamic range and modes of operation: Journal of Applied Geophysics, **33(1)**, 7–14.

Han, X., X. Tan, X. Li, Y. Pang, and L. Zhang, 2021, Water invasion performance of complex fracture-vuggy gas reservoirs based on classification modeling: Advances in Geo-Energy Research, **5**, 222–232.

Heigl, W. M., and M. Peeters, 2005, Can we obtain invasion depth with directional borehole radar?: Petrophysics, **46**, 52–61.

Hizem, M., H. Budan, B. Deville, O. Faivre, L. Mosse, and M. Simon, 2008, Dielectric dispersion: A new wireline petrophysical measurement: SPE Annual Technical Conference and Exhibition, SPE–116130–MS.

Huo, J., Q. Zhao, C. Ma, X. Sun, L. Wang, Y. Bo, X. Chang, and Y. Zhao, 2014, Design and tests of a borehole radar for oil well prospecting: Proceedings of the 15th International Conference on Ground Penetrating Radar, 798–802.

Huo, J., B. Zhou, I. M. Mason, and Q. Zhao, 2021, An application of reflected guided borehole radar waves to detection of subhorizontal structures: IEEE Transactions on Geoscience and Remote Sensing, **59**, 7201–7210.

Jang, H., S. Kuroda, and H. J. , Kim, 2011, Efficient electromagnetic imaging of an artificial infiltration process in the vadose zone using cross-borehole radar: IEEE Geoscience & Remote Sensing Letters, **8**, 243–247.

Jol, H., 2009, Ground penetrating radar: Theory and applications: Elsevier Science.

Klotzsche, A., L. Lärm, J. Vanderborght, G. Cai, S. Morandage, M. Zörner, H. Vereecken, and J. Kruk, 2019, Monitoring soil water content using time-lapse horizontal borehole GPR data at the field-plot scale: Vadose Zone Journal, **18**, 190044.

Liang, L., A. Abubakar, and T. M. Habashy, 2011, Estimating petrophysical parameters and average mud-filtrate invasion rates using joint inversion of induction logging and pressure transient data: Geophysics, **76**, no. 2, E21–E34.

Liu, S., 2014, Electromagnetic wave shielding and absorbing materials (in Chinese): Chemical Industry Press.

Liu, S., and M. Sato, 2002, Electromagnetic logging technique based on borehole radar: IEEE Transactions on Geoscience & Remote Sensing, **40**, 2083–2092.

Ma, C., Q. Zhao, J. Huo, X. Chang, and L. Ran, 2016, Single borehole radar for well logging in a limestone formation: Experiments and simulations: Journal of Environmental & Engineering Geophysics, **21**, 201–213.

Miorali, M., E. Slob, and R. Arts, 2011a, A feasibility study of borehole radar as a permanent downhole sensor: Geophysical Prospecting, **59**, 120–131.

Miorali, M., F. Zhou, E. Slob, and R. Arts, 2011b, Coupling ground penetrating radar and fluid flow modeling for oilfield monitoring applications: Geophysics, **76**, no. 3, A21–A25.

Navarro, D., 2007, Effects of invasion transient on resistivity time-lapsed logging: Master's thesis, University of Houston.

Ning, F., K. Zhang, N. Wu, L. Zhang, G. Li, G. Jiang, Y. Yu, L. Liu, and Y. Qin, 2013, Invasion of drilling mud into gas-hydrate-bearing sediments. Part I: effect of drilling mud properties: Geophysical Journal International, **193**, 1370–1384.

Oloumi, D., M. I. Pettersson, P. Mousavi, and K. Rambabu, 2015, Imaging of oil-well perforations using UWB synthetic aperture radar: IEEE Transactions on Geoscience & Remote Sensing, **53**, 4510–4520.

Pisani, P. D., and D. Vogt, 2004, Borehole radar delineation of the Ventersdorp Contact Reef in three dimensions: Exploration Geophysics, **35**, 319–323.

Salazar, J. M., and C. Torres-Verdín, 2008, Quantitative comparison of processes of oil- and water-based mud-filtrate invasion and corresponding effects on borehole resistivity measurements: Geophysics, **74**, no. 1, E57–E73.

Shenawi, S., J. White, E. Elrafie, and K. El-Kilany, 2007, Permeability and water saturation distribution by lithologic facies and hydraulic units: A reservoir simulation case study: SPE Middle East Oil and Gas Show and Conference, SPE–105273–MS.

Slob, E., M. Sato, and G. Olhoeft, 2010, Surface and borehole ground-penetrating-radar developments: Geophysics, **75**, no. 5, 75A103–75A120.

Torres-Verdín, C., F. O. Alpak, and T. M. Habashy, 2006, Petrophysical inversion of bore-hole array-induction logs: Part II–Field data examples: Geophysics, **71**, no. 5, G261–G268.

Tronicke, J., and G. Hamann, 2014, Vertical radar profiling: Combined analysis of travel-times, amplitudes, and reflections: Geophysics, **79**, no. 4, H23–H35.

Warren, C., A. Giannopoulos, and I. Giannakis, 2016, gprmax: Open source software to

simulate electromagnetic wave propagation for Ground Penetrating Radar: Computer Physics Communications, **209**, 163–170.

Wu, J., Torres-Verdin, K. Sepehrnoori, and M. A. Proett, 2005, The influence of water-base mud properties and petrophysical parameters on mudcake growth, filtrate invasion, and formation pressure: Petrophysics, **46**, 14–32.

Xia, Y., J. Cai, E. Perfect, W. Wei, Q. Zhang, and Q. Meng, 2019, Fractal dimension, lacunarity and succolarity analyses on ct images of reservoir rocks for permeability prediction: Journal of Hydrology, **579**, 124198.

Zhang, L., G. Liu, C. Zhou, and Z. Liu, 2005, Reservoir productivity prediction by array induction logging data: Petroleum Exploration & Development, **32**, 84–87.

Zhao, P., R. Qin, H. Pan, O. Mehdi, and W. Yuqi, 2019, Study on array laterolog response simulation and mud-filtrate invasion correction: Advances in Geo-Energy Research, **3**, 175–186.

Zhou, F., I. Giannakis, A. Giannopoulos, K. Holliger, and E. Slob, 2020, Estimating reservoir permeability with borehole radar: Geophysics, **85(4)**, no. 4, H51–H60.

Zhou, F., X. Hu, Q. Meng, X. Hu, and Z. Liu, 2015, Model and method of permeability evaluation based on mud invasion effects: Applied Geophysics, **12**, 482–492.

Zhou, F., Q. Meng, X. Hu, E. Slob, H. Pan, and H. Ma, 2016, Evaluation of reservoir permeability using array induction logging: Chinese Journal of Geophysics, **59**, 703–716.

Zhou, F., M. Miorali, E. Slob, and X. Hu, 2018, Reservoir monitoring using borehole radars to improve oil recovery: Suggestions from 3D electromagnetic and fluid modeling: Geophysics, **83(2)**, no. WB19–WB32.

Zhou, H., and M. Sato, 2004, Subsurface cavity imaging by crosshole borehole radar measurements: IEEE Transactions on Geoscience & Remote Sensing, **42**, 335–341.

1
2
3
4
5
6
7
8
9
10
11
12
13
14
15
16
17
18
19
20
21
22
23
24
25
26
27
28
29
30
31
32
33
34
35
36
37
38
39
40
41
42
43
44
45
46
47
48
49
50
51
52
53
54
55
56
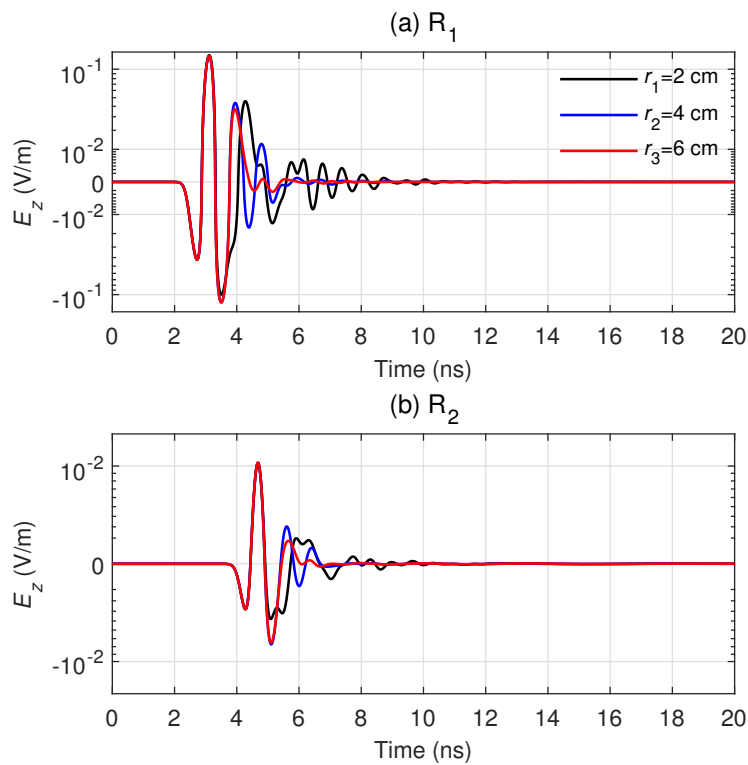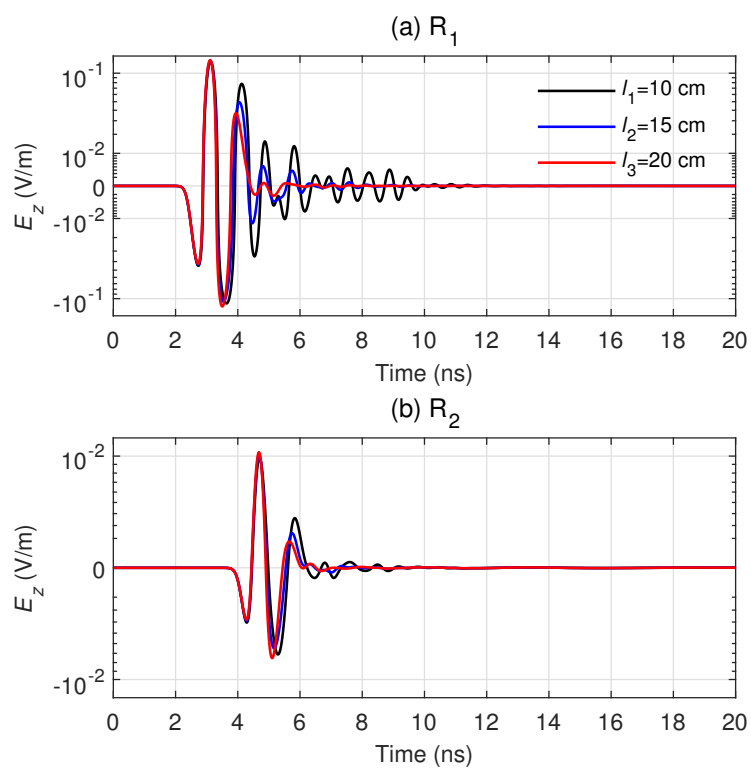57
58
59
60

LIST OF FIGURES

33

Figure 1: Overall structure (left) and geometric parameters (right) of the considered borehole radar model for simulation. The symbols T and $R_{1,2}$ denote the transmitting and receiving antennas, respectively.

Figure 2: Waveforms recorded by the (a) first and (b) second receiving antennas when the radial depth of the cavities is 2 cm (black curves), 4 cm (blue curves), and 6 cm (red curves), respectively. The symbols R_1 and R_2 denote the first and second receiving antennas, respectively.

1
2
3
4
5
6
7
8
9
10
11
12
13
14
15
16
17
18
19
20
21
22
23
24
25
26
27
28
29
30
31
32
33
34
35
36
37
38
39
40
41

Figure 3: Waveforms recorded by the (a) first and (b) second receiving antennas when the longitudinal length of the cavities is 10 cm (black curves), 15 cm (blue curves), and 20 cm (red curves), respectively. The symbols R_1 and R_2 denote the first and second receiving antennas, respectively.

42
43
44
45
46
47
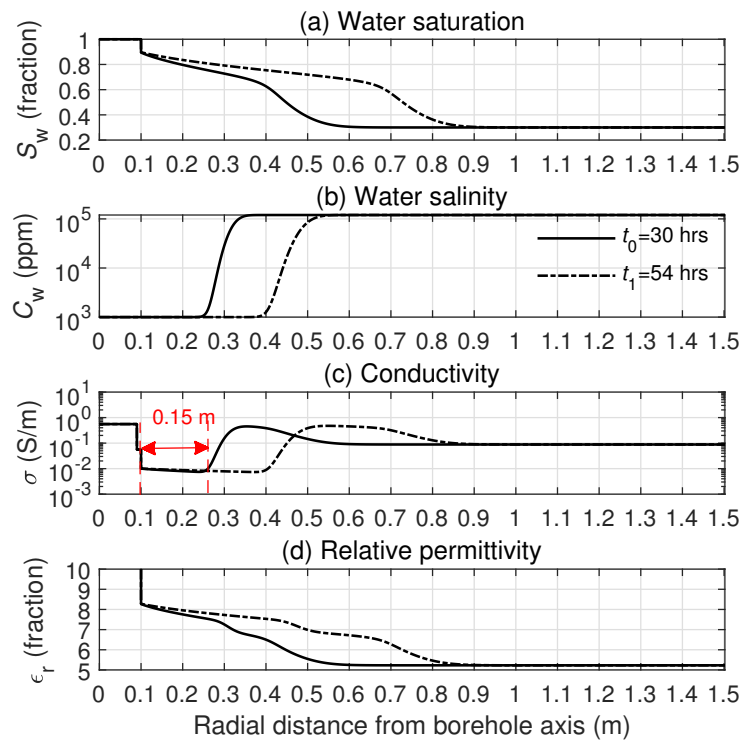48
49
50
51
52
53
54
55
56
57
58
59
60
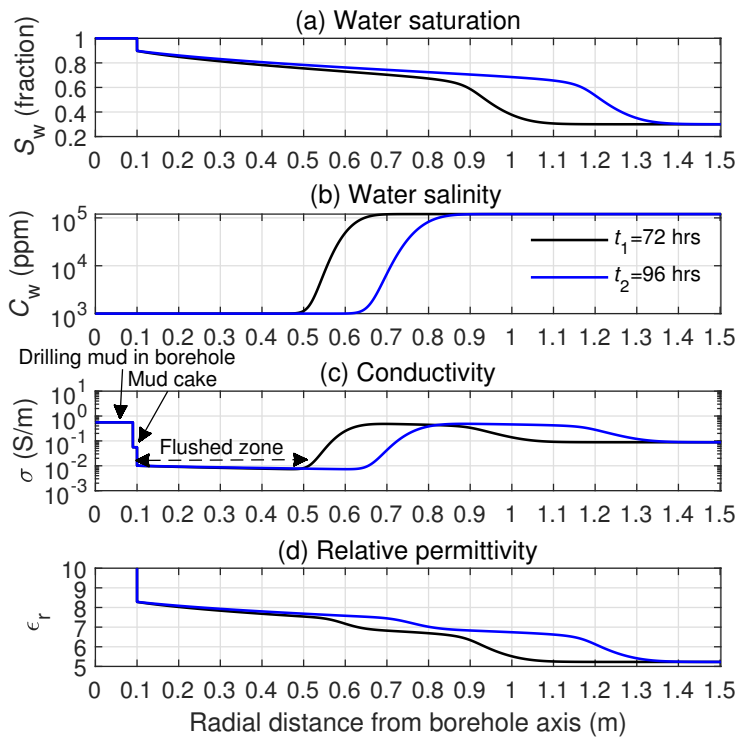
Figure 4: Radial distributions of (a) the water saturation, (b) the water salinity, (c) the bulk electrical conductivity, and (d) the bulk relative dielectric permittivity at an invasion time of 72 (black curves) and 96 (blue curves) hours, respectively.

1
2
3
4
5
6
7
8
9
10
11
12
13
14
15
16
17
18
19
20
21
22
23
24
25
26
27
28
29
30
31
32
33
34
35
36
37
38
39
40
41
42
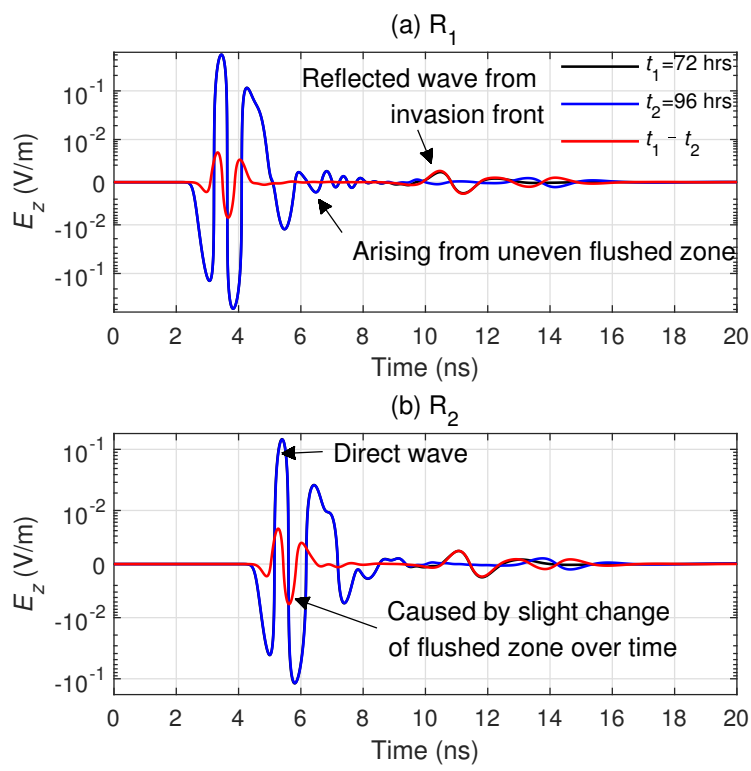
Figure 5: Radar signals recorded by the two receiving antennas (a) R_1 and (b) R_2 at an invasion time of 72 (black curves) and 96 (blue curves) hours, and their corresponding time-lapse signals (red curves).

43
44
45
46
47
48
49
50
51
52
53
54
55
56
57
58
59
60

1
2
3
4
5
6
7
8
9
10
11
12
13
14
15
16
17
18
19
20
21
22
23
24
25
26
27
28
29
30
31
32
33
34
35
36
37
38
39
40
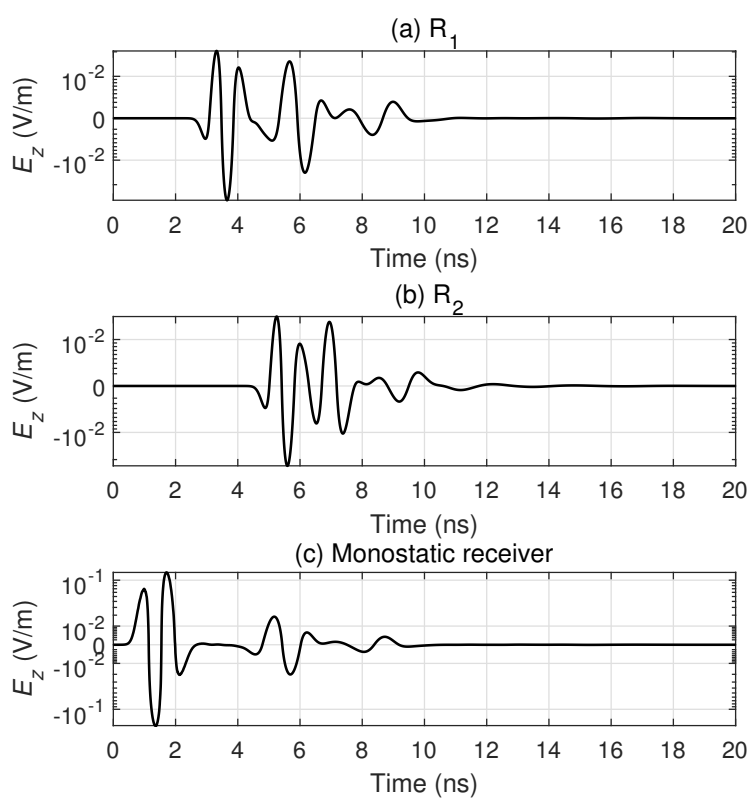41
42
43
44
45
46
47
48
49
50
51
52
53
54
55
56
57
58
59
60
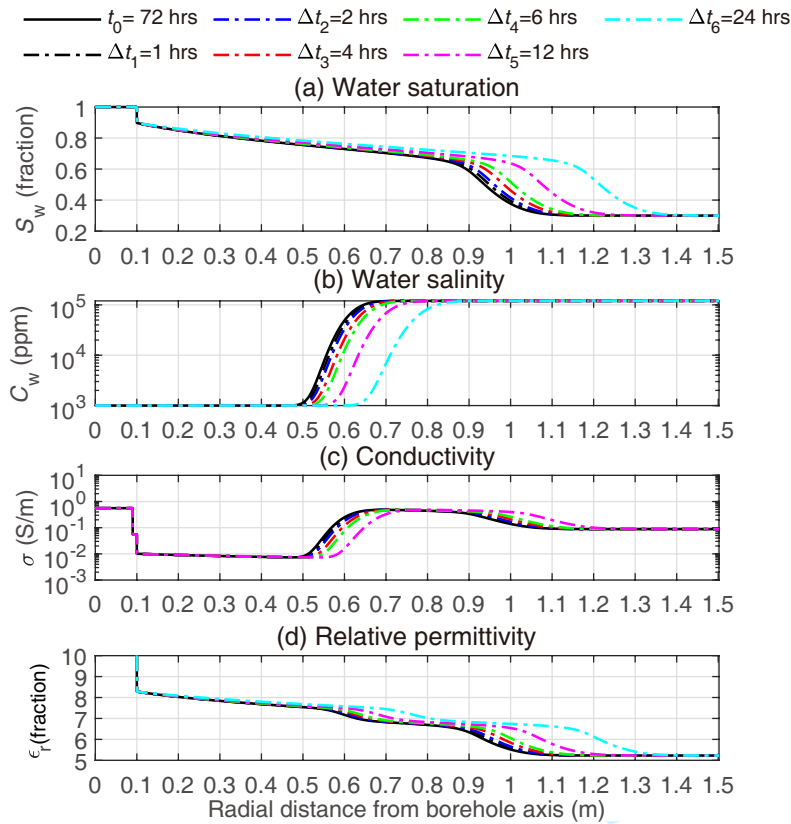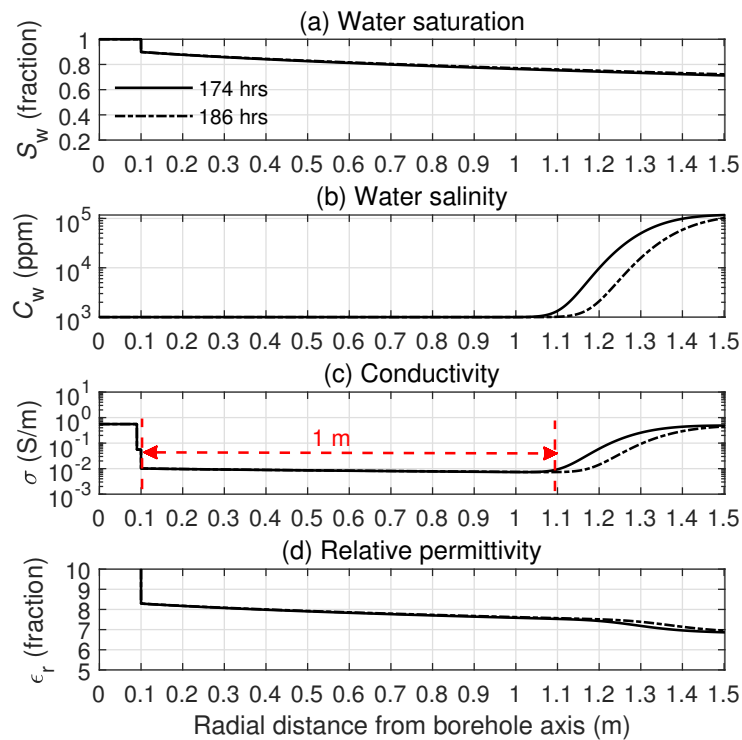

Figure 6: Radial distributions of (a) the water saturation, (b) the water salinity, (c) the bulk electrical conductivity, and (d) the bulk relative dielectric permittivity in time-lapse borehole radar measurements. The first measurement time (t_0) is at an invasion of 72 hours (black curves), and the lag time (Δt) of the second measurement is 1 (black dashed curves), 2 (blue dashed curves), 4 (red dashed curves), 6 (green dashed curves), 12 (magenta dashed curves), and 24 (cyan dashed curves) hours, respectively.

1
2
3
4
5
6
7
8
9
10
11
12
13
14
15
16
17
18
19
20
21
22
23
24
25
26
27
28
29
30
31
32
33
34
35
36
37
38
39
40
41
42
43
44
45
46
47
48
49
50
51
52
53
54
55
56
57
58
59
60
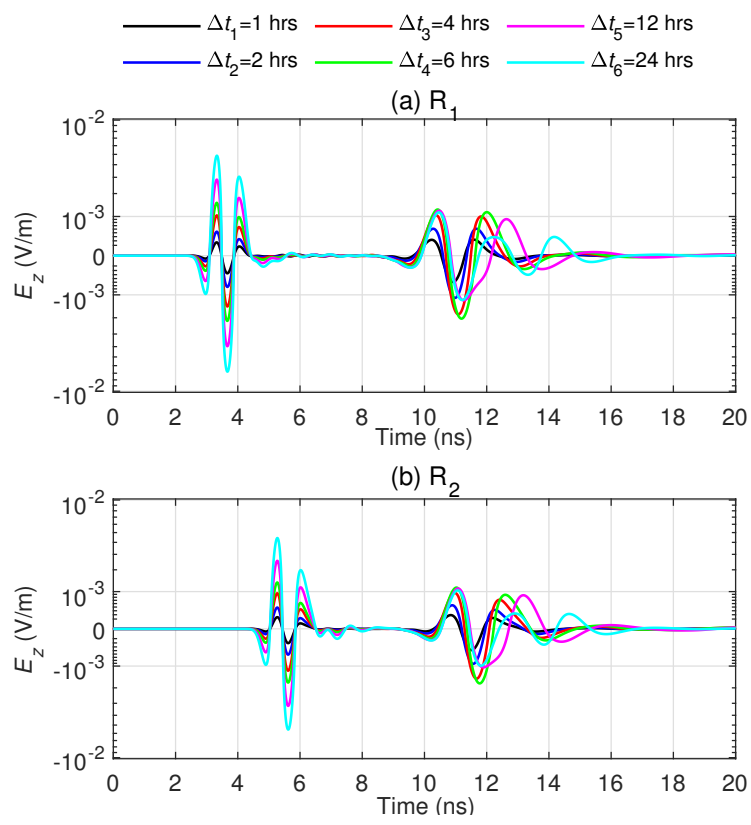
Figure 7: Time-lapse radar signals recorded by (a) R_1 and (b) R_2 for varying lag times, corresponding to the fluid distributions in Figure 6.

Figure 8: Radial distributions of (a) the water saturation, (b) the water salinity, (c) the bulk electrical conductivity, and (d) the bulk relative dielectric permittivity at an invasion time of 30 (solid curves) and 54 (dashed curves) hours. The red line indicates the minimum detection range of the time-lapse borehole radar for the invasion front from the borehole wall.

Figure 9: Time-lapse radar signals recorded by (a) R_1, (b) R_2, and (c) monostatic (zero-offset) antenna configurations, corresponding to the fluid distributions in Figure 8.
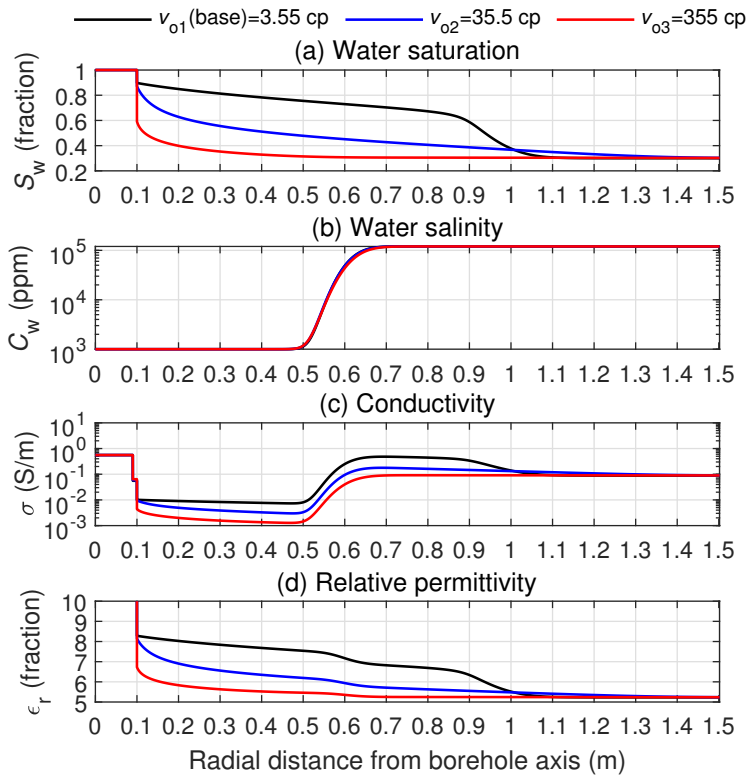
Figure 10: Radial distributions of (a) the water saturation, (b) the water salinity, (c) the bulk electrical conductivity, and (d) the bulk relative dielectric permittivity at an invasion time of 174 (solid curves) and 186 (dashed curves) hours. The red line indicates the maximum detection range of the time-lapse borehole radar for invasion front from the borehole wall.
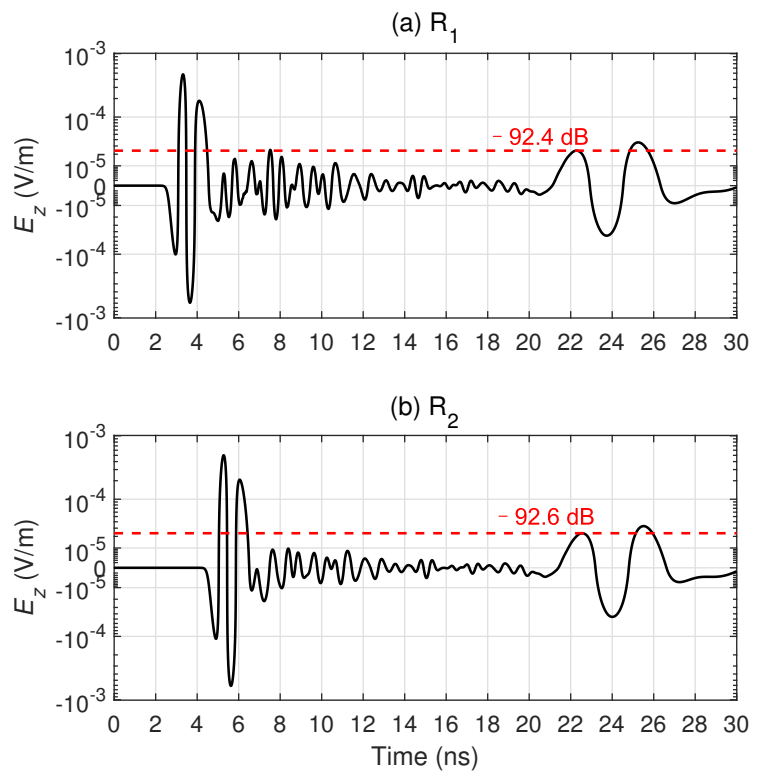
Figure 11: Time-lapse radar signals recorded by the receiving antennas (a) R_1 and (b) R_2, corresponding to the fluid distributions in Figure 10. The red dashed lines indicate the logarithmic expression of the amplitude relative to the maximum amplitude of 1 V/m, thus quantifying the required dynamic range for detecting the reflected signals.
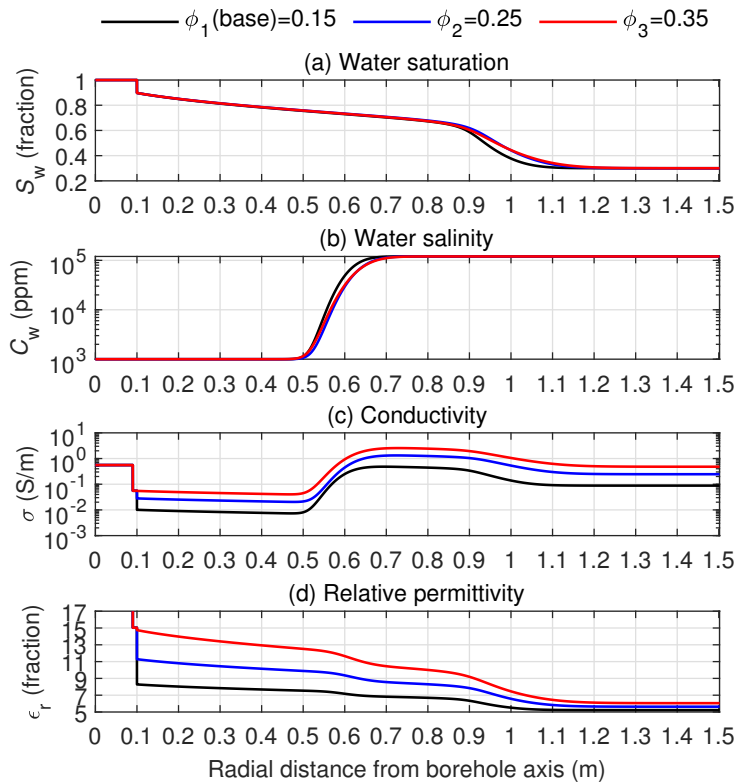
Figure 12: Radial distributions of (a) the water saturation, (b) the water salinity, (c) the bulk electrical conductivity, and (d) the bulk relative dielectric permittivity when the mud front has a distance of 0.4 m from the borehole wall. The oil viscosity is 3.55 (black curves), 35.5 (blue curves), and 355 (red curves) cp, respectively.
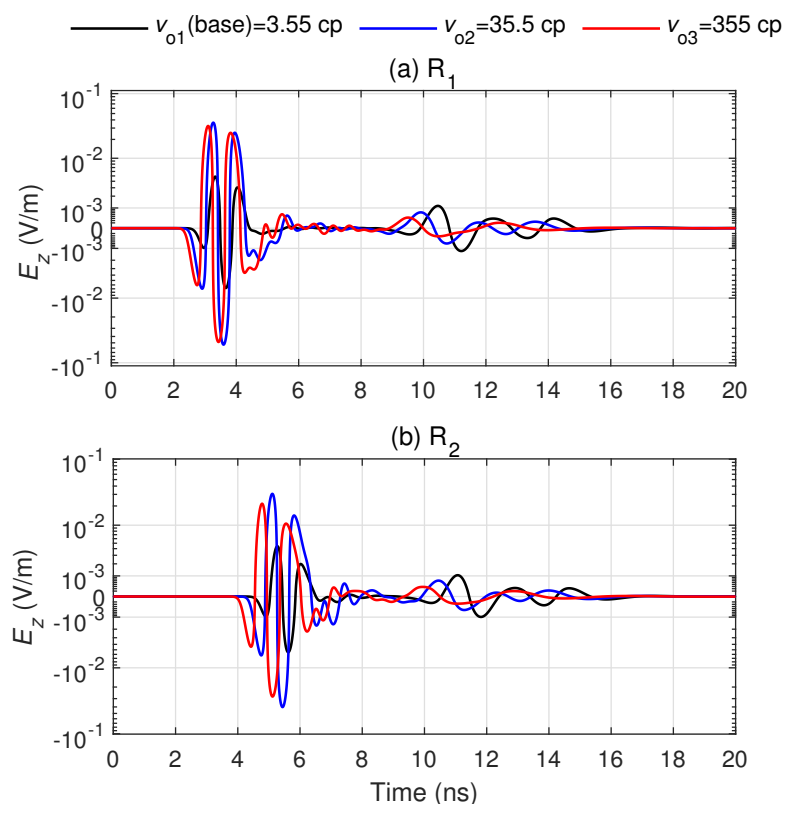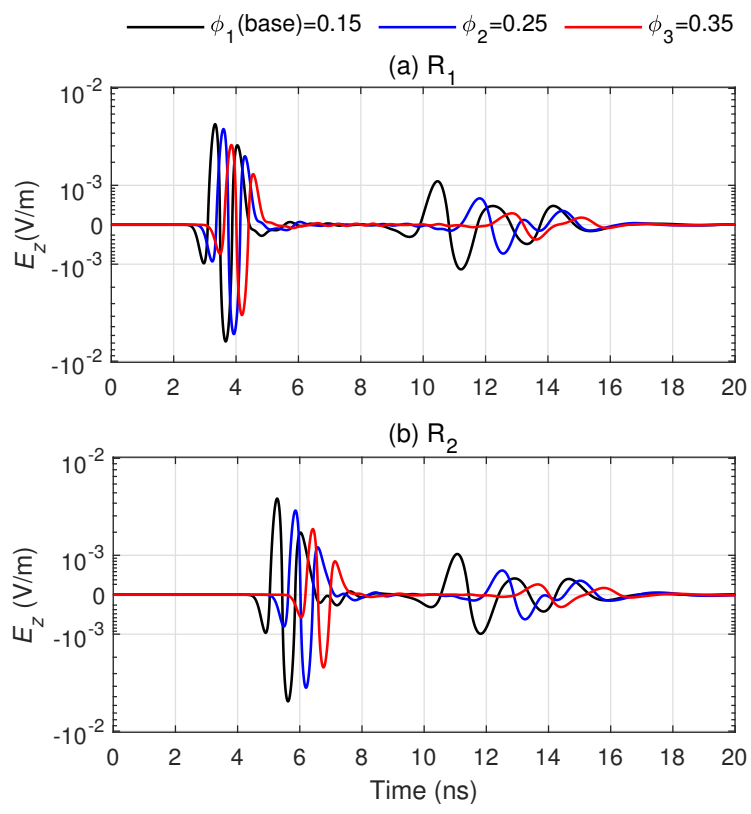
Figure 13: Time-lapse radar signals recorded by (a) R_1 and (b) R_2 corresponding to the simulated fluid distributions in Figure 12.

Figure 14: Radial distributions of (a) the water saturation, (b) the water salinity, (c) the bulk electrical conductivity, and (d) the bulk relative dielectric permittivity when the mud front has a distance of 0.4 m from the borehole wall. The porosity is 0.15 (black curves), 0.25 (blue curves), and 0.35 (red curves), respectively.

Figure 15: Time-lapse radar signals recorded by (a) R_1 and (b) R_2 corresponding to the simulated fluid distributions in Figure 14.
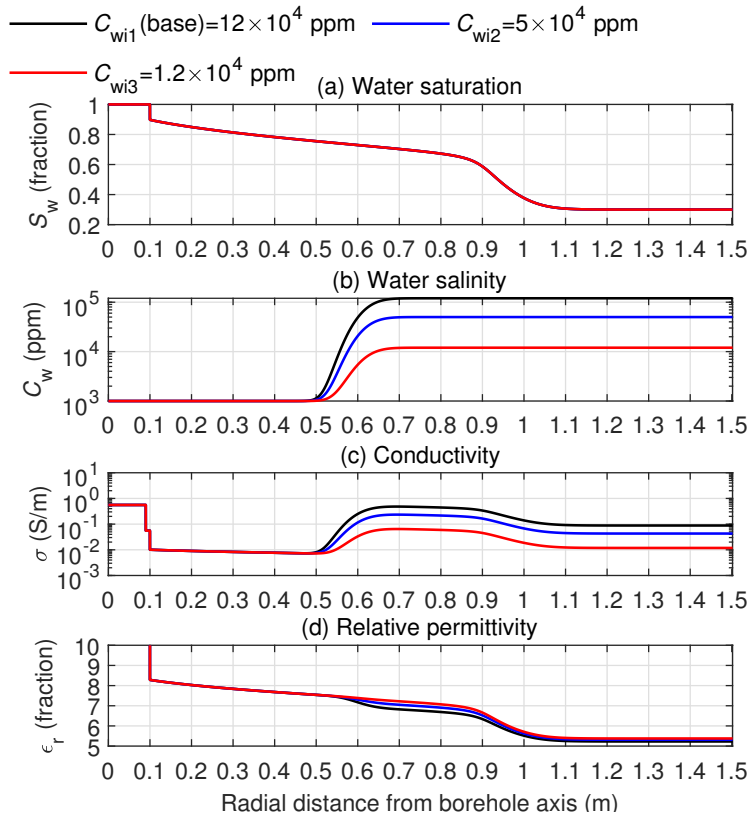
Figure 16: Radial distributions of (a) the water saturation, (b) the water salinity, (c) the bulk electrical conductivity, and (d) the bulk relative dielectric permittivity when the mud front has a distance of 0.4 m from the borehole wall. The initial formation water salinity is 12×10^4 (black curves), 5×10^4 (blue curves), and 1.2×10^4 (red curves) ppm, respectively.
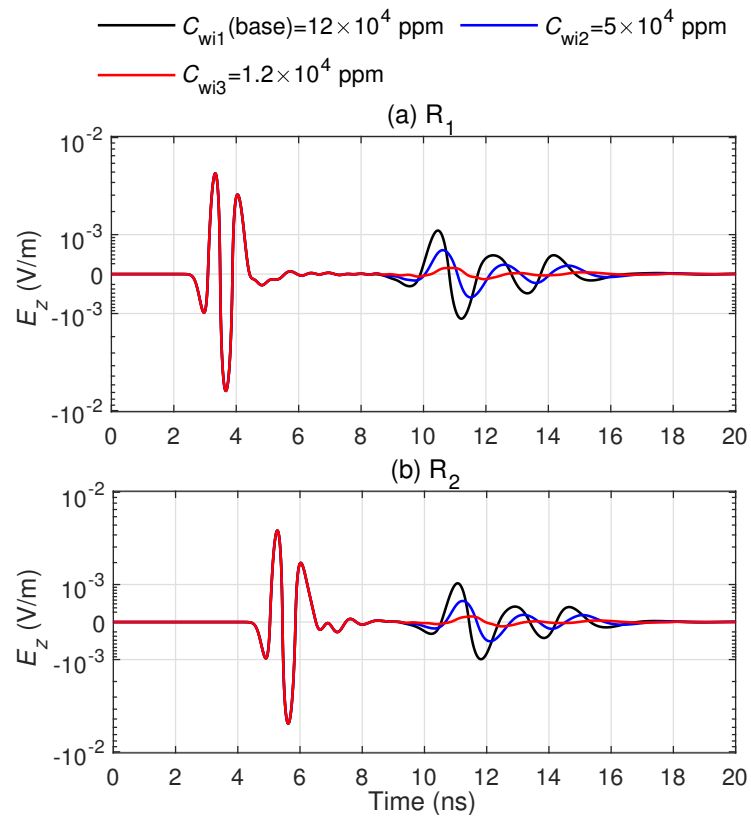
Figure 17: Time-lapse radar signals recorded by (a) R_1 and (b) R_2 corresponding to the simulated fluid distributions in Figure 16.

Figure 18: (a) Heterogeneous porosity distribution for a fractal dimension of 1, and the associated distributions of (b) bulk relative dielectric permittivity and (c) bulk electric conductivity, when the mud invasion front is 0.4 m away from the borehole wall.
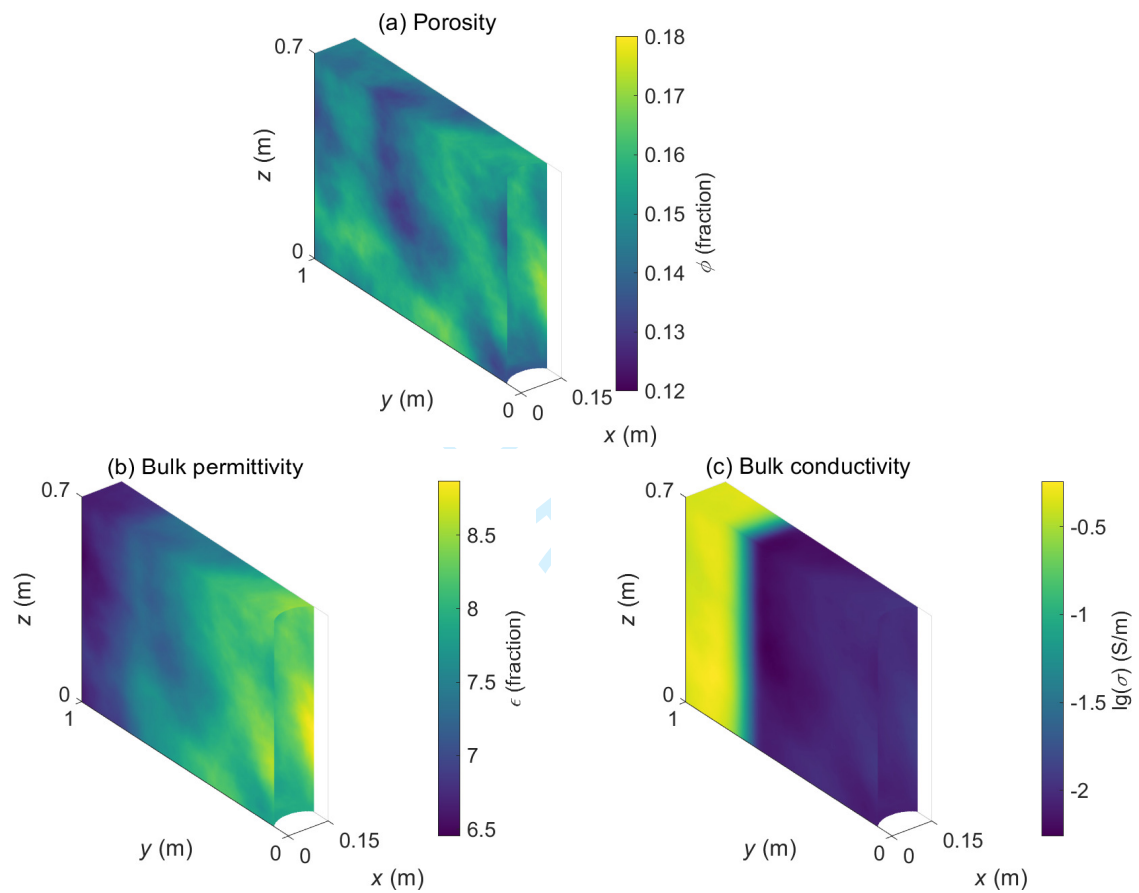
Figure 19: (a) Heterogeneous porosity distribution for a fractal dimension of 2, and the associated distributions of (b) bulk relative dielectric permittivity and (c) bulk electric conductivity, when the mud invasion front is 0.4 m away from the borehole wall.

Figure 20: (a) Heterogeneous porosity distribution for a fractal dimension of 3, and the associated distributions of (b) bulk relative dielectric permittivity and (c) bulk electric conductivity when the mud invasion front is 0.4 m away from the borehole wall.

1
2
3
4
5
6
7
8
9
10
11
12
13
14
15
16
17
18
19
20
21
22
23
24
25
26
27
28
29
30
31
32
33
34
35
36
37
38
39
40
41
42
43
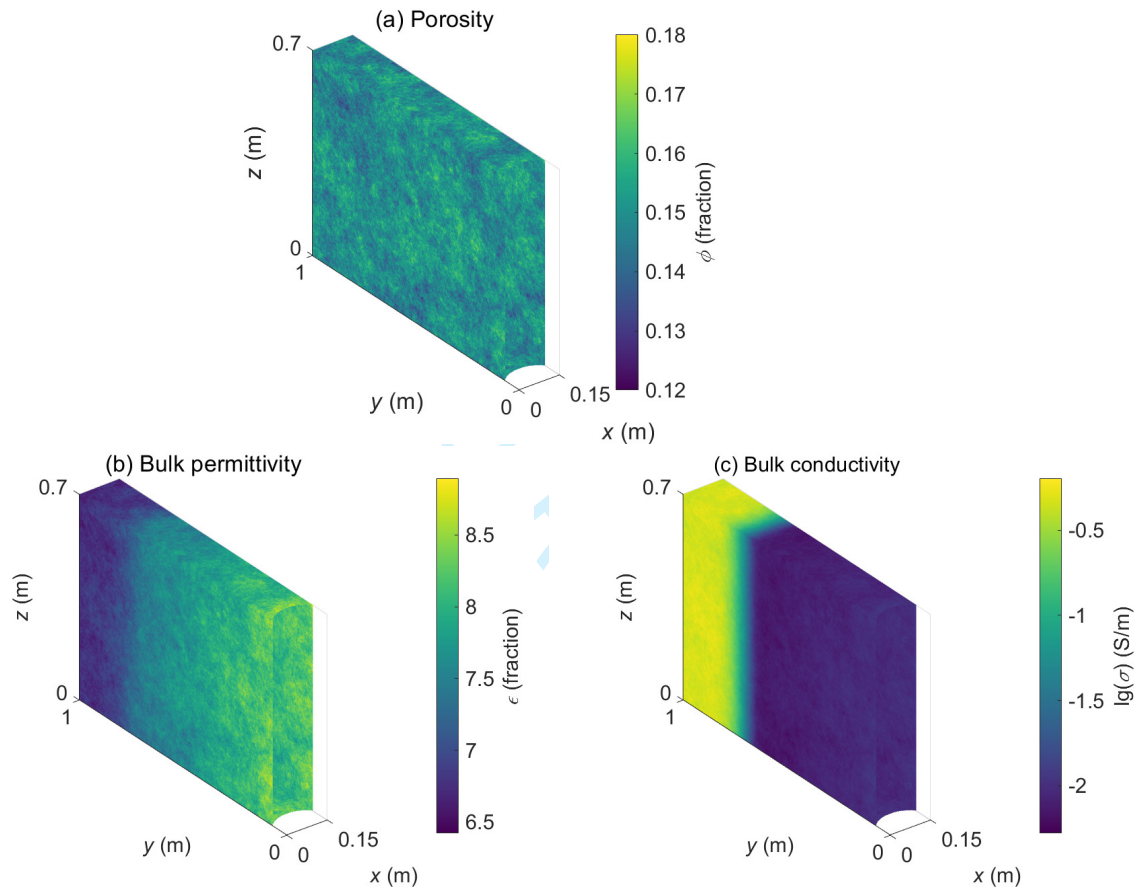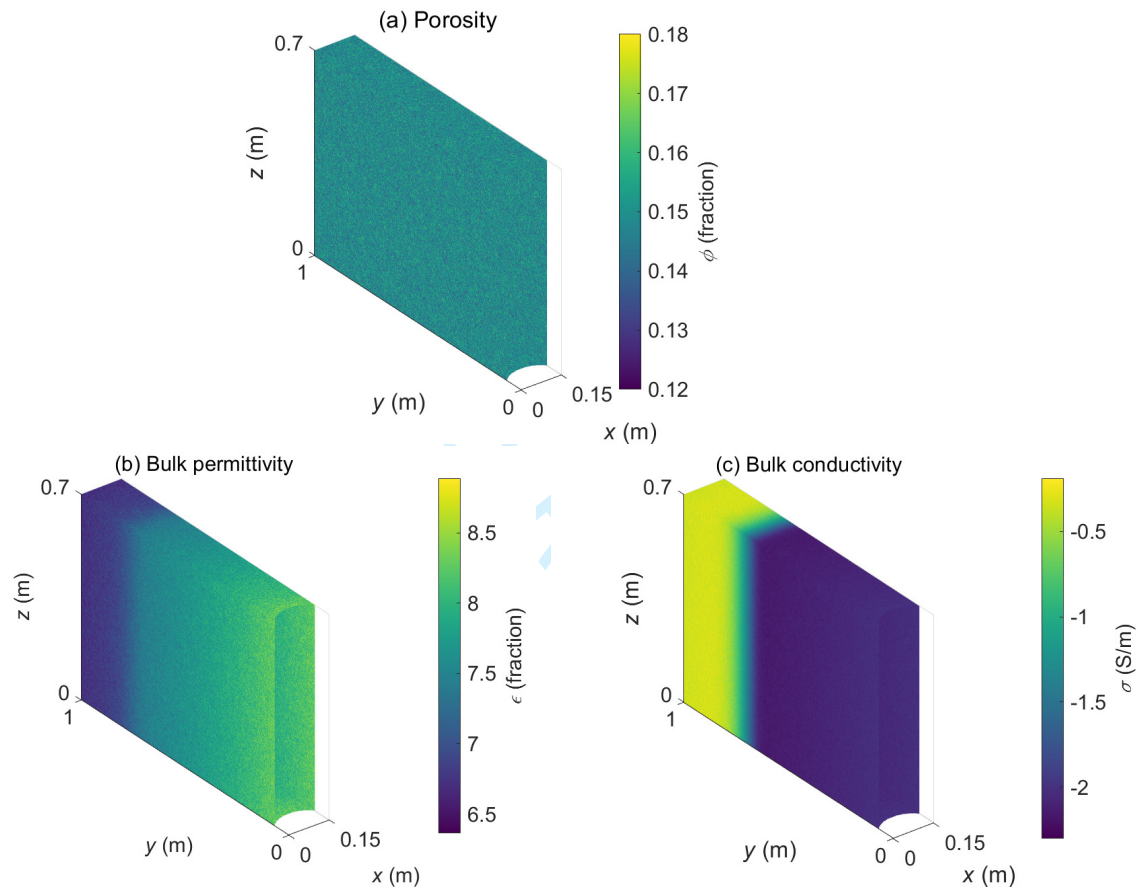44
45
46
47
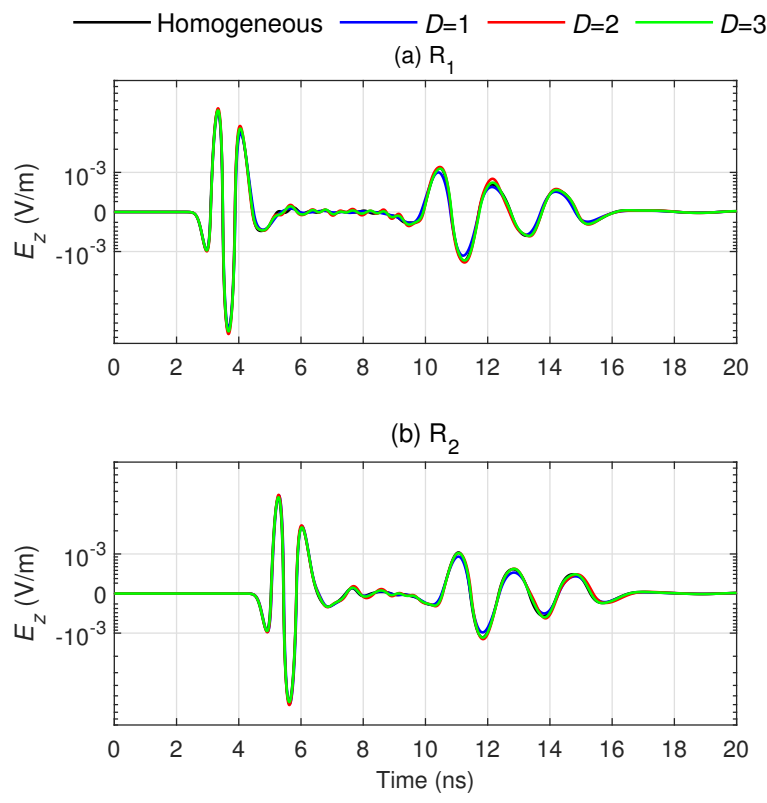48
49
50
51
52
53
54
55
56
57
58
59
60

Figure 21: Time-lapse signals recorded by the receiving antennas (a) R_1 and (b) R_2(b) for the heterogeneous reservoir models in Figures 18 (blue curves), 19 (red curves), 20 (green curves), and the homogeneous reference model (black curves), respectively. The symbol D denotes the fractal dimension.

LIST OF TABLES

Table 1: Fluid, rock and borehole properties for the reservoir scenario considered in this study (Alpak et al., 2006; Navarro, 2007; Hizem et al., 2008; Salazar and Torres-Verdín, 2008; Liang et al., 2011)

Variables	*Values*	*Units*
Water density	1001	kg/m^3
Oil density	816	kg/m^3
Water viscosity	1.274×10^{-3}	Pa·s
Oil viscosity	3.550×10^{-3}	Pa·s
Rock compressibility	0.725×10^{-12}	1/Pa
Water compressibility	0.369×10^{-9}	1/Pa
Oil compressibility	2.762×10^{-9}	1/Pa
Gravitational acceleration	9.800	m/s^2
Reservoir pressure	20.684×10^6	Pa
Bottomhole pressure	24.821×10^6	Pa
Formation water salinity	120×10^3	ppm
Mud filtrate salinity	1×10^3	ppm
Borehole radius	0.100	m
Ionic diffusion coefficient	6.452×10^{-9}	m^2/s
Dispersion coefficient	1.300×10^{-3}	m
Connate water saturation	0.15	fraction
Residual oil saturation	0.10	fraction
End-point value of relative permeability of water	0.30	fraction
End-point value of relative permeability of oil	1	fraction
Corey exponent of water	2.00	dimensionless
Corey exponent of oil	2.00	dimensionless
Capillary pressure coefficient	18.70×10^{-3}	Pa·m
Empirical exponent for pore-size distribution	5.00	dimensionless
Referenced permeability of mud cake	0.01	md
Referenced porosity of mud cake	0.40	fraction
Pressure difference between borehole and formation	4	MPa
Maximum thickness of mud cake	0.01	m
Volumetric fraction of solid particles in mud	0.50	fraction
Compressibility exponent of mud cake	0.40	fraction
Exponent multiplier of mud cake	0.10	fraction
Reservoir temperature	93.3	°C
Relative permittivity of oil	2	dimensionless
Relative permittivity of water	57.93	dimensionless
Relative permittivity of rock matric	4.65	dimensionless
Tortuosity factor	1	dimensionless
Cementation exponent	2	dimensionless
Saturation exponent	2	dimensionless

Table 2: Geometric parameters and dielectric properties of the simulated borehole radar logging tool.

Variables	Values	Units
Logging string radius	0.050	m
First transmitter−receiver spacing	0.200	m
Second transmitter−receiver spacing	0.400	m
Radial depth of cavity	0.060 (after optimization)	m
Longitudinal length of cavity	0.200 (after optimization)	m
Relative permittivity of absorbing material	20-9i	dimensionless
Relative magnetic permeability of absorbing material	1.200-12i	dimensionless

1
2
3
4
5
6
7
8
9
10
11
12
13
14
15
16
17
18
19
20
21
22
23
24
25
26
27
28
29
30
31
32
33
34
35
36
37
38
39
40
41
42
43
44
45
46
47
48
49
50
51
52
53
54
55
56
57
58
59
60

Table 3: Qualitative classification of the influence of various petrophysical properties.

Variables	*Major*	*Minor*
Oil viscosity	$\sqrt{}$	-
Porosity	$\sqrt{}$	-
Mud salinity	$\sqrt{}$	-
Formation water salinity	$\sqrt{}$	-
Molecular diffusion coefficient	$\sqrt{}$	-
Cementation exponent	$\sqrt{}$	-
Initial water saturation	-	$\sqrt{}$
Relative permeability	-	$\sqrt{}$
Capillary pressure	-	$\sqrt{}$
Saturation exponent	-	$\sqrt{}$
Heterogeneity	-	$\sqrt{}$